Computers in Biology and Medicine 146 (2022) 105511

Contents lists available at ScienceDirect

Computers in Biology and Medicine

journal homepage: www.elsevier.com/locate/compbiomed

Modeling the efficacy of different anti-angiogenic drugs on treatment of solid tumors using 3D computational modeling and machine learning

Milad Mousavi [a], Mahsa Dehghan Manshadi [a,q], Madjid Soltani [b,c,q,**], Farshad M. Kashkooli [d,q], Arman Rahmim [e,f], Amir Mosavi [g,k,m,*], Michal Kvasnica [m], Peter M. Atkinson [h,n,o,p], Levente Kovács [i,j], Andras Koltay [k], Norbert Kiss [k], Hojjat Adeli [l]

[a] Cancer Institute of Iran, Tehran University of Medical Sciences (TUMS), Tehran, Iran
[b] Department of Electrical and Computer Engineering, University of Waterloo, Ontario, Canada
[c] Centre for Biotechnology and Bioengineering (CBB), University of Waterloo, Waterloo, Ontario, Canada
[d] Department of Physics, Ryerson University, Toronto, ON, Canada
[e] Department of Radiology and Physics, University of British Columbia, Vancouver, BC, Canada
[f] Department of Integrative Oncology, BC Cancer Research Institute, Vancouver, BC, Canada
[g] Institute of Software Design and Development, Obuda University, 1034, Budapest, Hungary
[h] Faculty of Science and Technology, Lancaster University, Lancaster, UK
[i] Biomatics Institute, John von Neumann Faculty of Informatics, Obuda University, 1034, Budapest, Hungary
[j] Physiological Controls Research Center, University Research and Innovation Center, Obuda University, 1034, Budapest, Hungary
[k] National University of Public Service, Budapest, Hungary
[l] Department of Biomedical Informatics and Neuroscience, The Ohio State University, Columbus, OH, 43220, USA
[m] Institute of Information Engineering, Automation and Mathematics, Slovak University of Technology in Bratislava, Bratislava, Slovakia
[n] Geography and Environmental Science, University of Southampton, Highfield, Southampton SO17 1BJ, UK
[o] Institute of Geographic Sciences and Natural Resources Research, Chinese Academy of Sciences, 11A Datun Road, Beijing 100101, China
[p] Lancaster Environment Centre, Lancaster University, Bailrigg, Lancaster LA1 4YR, UK
[q] Department of Mechanical Engineering, K. N. Toosi University of Technology, Tehran 1999143344, Iran

ARTICLE INFO

Keywords:
Solid tumor
Tumor growth
Anti-angiogenic drugs
Bevacizumab
Ranibizumab
Brolucizumab
Artificial intelligence
Cancer

ABSTRACT

Accurate simulation of tumor growth during chemotherapy has significant potential to alleviate the risk of unknown side effects and optimize clinical trials. In this study, a 3D simulation model encompassing angiogenesis and tumor growth was developed to identify the vascular endothelial growth factor (VEGF) concentration and visualize the formation of a microvascular network. Accordingly, three anti-angiogenic drugs (Bevacizumab, Ranibizumab, and Brolucizumab) at different concentrations were evaluated in terms of their efficacy. Moreover, comprehensive mechanisms of tumor cell proliferation and endothelial cell angiogenesis are proposed to provide accurate predictions for optimizing drug treatments. The evaluation of simulation output data can extract additional features such as tumor volume, tumor cell number, and the length of new vessels using machine learning (ML) techniques. These were investigated to examine the different stages of tumor growth and the efficacy of different drugs. The results indicate that brolucizuman has the best efficacy by decreasing the length of sprouting new vessels by up to 16%. The optimal concentration was obtained at 10 mol m^{-3} with an effectiveness percentage of 42% at 20 days post-treatment. Furthermore, by performing comparative analysis, the best ML method (matching the performance of the reference simulations) was identified as reinforcement learning with a 3.3% mean absolute error (MAE) and an average accuracy of 94.3%.

1. Introduction

Anti-angiogenic drugs have been the subject of significant research and many trials for their efficacy in treating solid tumors. Oncogenic progression in solid tumors relies on new microvessels sprouting from existing vessels, known as tumor angiogenesis, to supply oxygen and

* Corresponding author. Obuda University, Hungary.
** Corresponding author. Department of Electrical and Computer Engineering, University of Waterloo, Ontario, Canada.
E-mail address: amir.mosavi@uni-obuda.hu (A. Mosavi).

https://doi.org/10.1016/j.compbiomed.2022.105511
Received 22 December 2021; Received in revised form 6 April 2022; Accepted 7 April 2022
Available online 18 April 2022

Table 1
Examples of research utilizing AI for tumor growth modeling.

Reference	Description	Journal/Year	Analysis method	Dataset	Remarks
Przedborski et al. [71]	Systems biology informed neural networks (SBINN) predict response and novel combinations for PD-1 checkpoint blockade	Communications Biology/2021	Systems biology informed neural networks (SBINN)	Ex-vivo dataset with 37 patients	The method aids in the development of targeted experiments for patient drug screening and identifying novel therapeutic targets.
Yazdjerdi et al. [72]	Reinforcement learning-based control of tumor growth under anti-angiogenic therapy	Computer Methods and Programs in Biomedicine/2020	Q-learning algorithm (reinforcement)	Obtained from mathematical modeling	The proposed reinforcement learning controller for cancer treatment utilizes anti-angiogenic treatment to identify effective and novel results.
Zwep et al. [23]	Identification of high-dimensional omics-derived predictors for tumor growth dynamics using machine learning and pharmacometric modeling	Pharmacometrics and Systems Pharmacology/2021	Machine learning and pharmacometric modeling	4,000 PDX from of 277 patients	Combining machine learning and pharmacometric modeling can be used to gain pharmacological understanding in genomic factors in treatment response.
Tang et al. [22]	Image-based classification of tumor type and growth rate using machine learning: a preclinical study	Scientific Reports/ 2019	Different machine learning methods including decision tree, random forest, and support vector machine	87 images	Predictive models can utilize standard medical images for classification and prediction of tumor types. Using this model, some parameters such as gray-level co-occurrence matrix (GLCM) size, tumor region, and tumor type were investigated.
Mascheroni et al. [24]	Bayesian combination of mechanistic modeling and machine learning (BaM3): improving clinical tumor growth predictions	Communications Medicine/2021	Mathematical modeling and machine learning	N-patient ensemble dataset	Combining two different approaches results in predictions improvement in all patients.
Heydarpour et al. [73]	Solving an optimal control problem of cancer treatment by artificial neural networks	International Journal of Interactive Multimedia &/2020	Artificial neural network	Obtained from mathematical simulation	They investigated optimal dose of chemotherapy drug and its concentration in the treatment process.

nutrients and remove metabolic waste [1–3]. The Folkman hypothesis states that new blood vessels sprout from parent vessels when cell proliferation and hypoxia occur, secrete tumor angiogenesis factor (TAF) [4]. The stimulation of blood vessels induces angiogenesis induction by one of the essential TAFs, the vascular endothelial growth factor (VEGF) [5]. After the avascular stages of tumor growth (tumor size of approximately 1 mm), vascular steps emerge through angiogenesis, the most critical factor in tumor progression [6]. Amongst current developments and different approaches in cancer therapeutics, anti-angiogenic drugs produce promising outcomes [7,8].

Although there has been a rapid increase in the number of clinical trials on anti-angiogenic drugs, there have been challenges due to inefficient trial design, recruitment and data collection difficulties, and complexity in maintaining and monitoring expensive laboratory experiments [9,10]. Researchers have evaluated mathematical models based on underlying biological properties to understand better the various processes involved in drug development and preclinical evaluation [11–15]. The advantage of this approach is that the biological features of the drugs can be tested by changing the parameters values of the models. The current research focuses on the three-dimensional simulation of tumor growth, with and without a prescription, to identify the differential benefits of the anti-angiogenic drugs bevacizumab, ranibizumab, and brolucizumab and their efficacy in inhibiting tumor growth. Vilanova et al. [16] studied a combination of computational and imaging models of tumor-induced angiogenesis using graph theory [17–19] to overcome some challenges in tumor growth treatment.

Additionally, Tang et al. [20] developed pressure-based 3D computational modeling of tumor growth and angiogenesis to evaluate chemotherapy drug responses. Their mathematical modeling indicated that solid tumor shape is related to interstitial fluid pressure, resulting in different tumor geometries. They studied different Avastin concentrations and assessed their distribution and tumor morphology. Yanagisawa et al. [21] applied a mathematical-based simulation that considered angiopoietin as an essential factor in vessel growth during angiogenesis.

1.1. Mathematical background

ML is a type of Artificial Intelligence (AI) method that permits the computer to contain some information without any explicit programs. The most significant contribution of the ML method is to prepare the artificial brains to start learning procedures without any human assistance. ML has consisted chiefly of three approaching groups called supervised, unsupervised, and reinforcement learning. Supervised learning needs someone to prepare input and required output as a dataset, with respect to providing reaction as it is called feedback about the learning accuracy within the training procedure. On the other hand, unsupervised learning does not need any training steps. The other group is reinforcement learning which is entirely related to training about the correct and false answers.

Artificial intelligence (AI)-based machine learning (ML) methods are appropriate for modeling the intrinsic complexities of biomedical systems without explicit knowledge of underlying interactions. While mathematical modeling is dependent on causality, statistical and ML methods determine the correlations from the data themselves [22,23], facilitating the systematic processing of big data and the inference of hidden patterns relating to biological problems. Thus, while AI-based methods can potentially provide high predictive accuracy given appropriate training, they usually do not provide any mechanistic perspective on the problem [24]. A general understanding of the basic dynamics of the system is almost impossible as an opportunity to generalize the behavior of the “learned” system. To meet these two challenges with the ultimate goal of increasing the accuracy of predictions, the authors present a predictive method that combines mathematical modeling and ML. As a proof of concept, the proposed method was tested on artificial datasets of tumor growth. Adeli et al. [25] advanced a multi-paradigm approach for automated electroencephalogram (EEG)-based diagnosis of various neurological and psychiatric disorders through adroit integration of signal processing techniques such as wavelets [26,27], nonlinear science/chaos theory [28], and neural network/machine learning [29]. These disorders include epilepsy and seizure detection [30–33], Alzheimer’s disease (AD) [34], mild cognitive impairment (MCI) [35–38], Parkinson’s disease [39–43], dementia classification

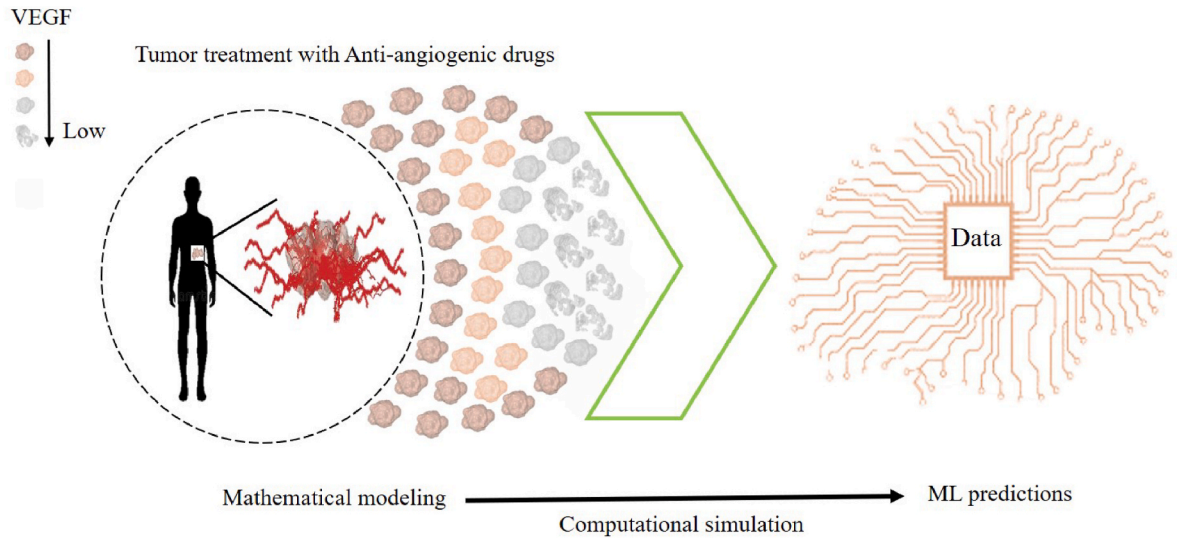

Fig. 1. Overview of the presented methodology and data employed in this work.

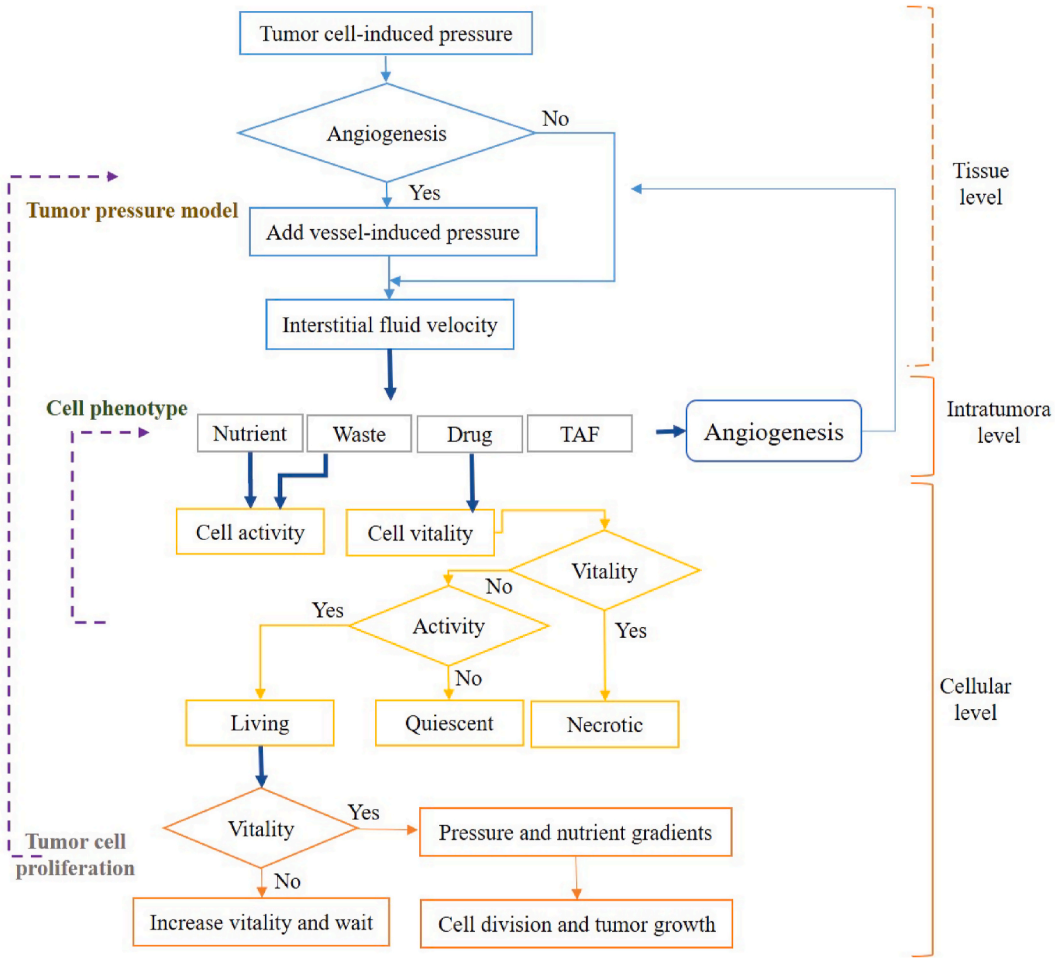

Fig. 2. A step-by-step flowchart of the employed multiscale mathematical modeling of tumor growth.

[44,45], autism spectrum disorder (ASD) [46,47], major depressive disorder (MDD) [48–51], bipolar disorder [52], attention deficit hyperactivity disorder (ADHD) [53], schizophrenia [54], alcoholism [55] and sleep stage classification [56,57]. This research on developing novel algorithms is intended to transform the practice of neurology and psychology [58]. Hassanpour et al. [59] presented an end-to-end deep learning methodology for classifying multiclass motor imagery EEG signals for brain-computer interface (BCI) applications. Recently, several authors have employed deep neural networks such as convolutional neural networks (CNNs) for epilepsy diagnosis [60,61], seizure detection [62,63], seizure prediction [64], seizure control [65], autism diagnosis [66] and autism prediction [67]. Mirzaei et al. [68] reviewed

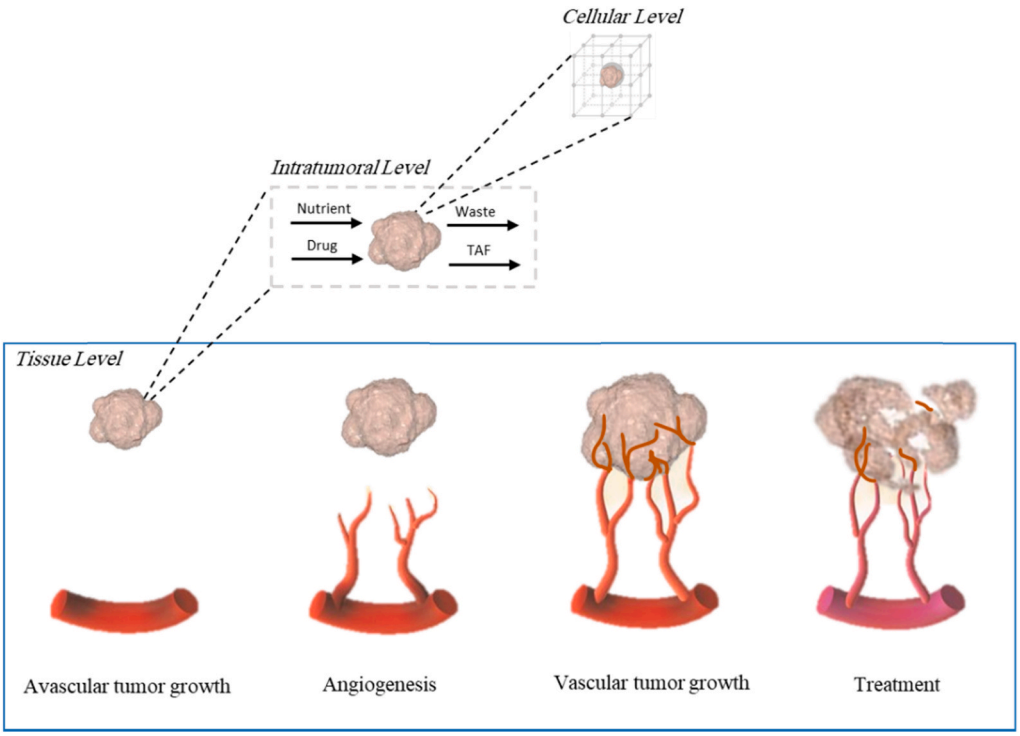

Fig. 3. The detailed information about each scale of the tumor growth.

imaging and machine learning approaches to diagnose AD. A review of AI techniques for automated diagnosis of neurological disorders was presented by Raghavendra et al. [69]. A comprehensive review of ML methods and statistical analysis for EEG-based diagnosis of AD was recently presented by Tzimourta et al. [70].

ML methods have the potential to increase the accuracy of prediction for different biological systems, including biological factors of tumor growth, as demonstrated by the reviewed examples in Table 1. Following a comprehensive literature review on this issue, the authors concluded that the feature extraction of several critical parameters should be investigated during the drug administration procedure to monitor drug effects on tumor cells. Consequently, advances in computational methods, notably ML, have made it possible to simulate the effects of different anti-angiogenic drugs on solid tumors, potentially leading to improvements in clinical trials.

In medical based cancer prediction researches, Stadlbauer et al. has evaluated the potential for the development of high-performance decision support tools of precision oncology with reinforcement learning methods [74]. Another research by Yala et al. has done with this method in order to the breast cancer monitoring and prediction [75]. In the random forest application, Feng et al. analyzed multicategory outcomes of colorectal cancer [76] and long short-term memory (LSTM) [37, 77–79], were employed in this study to examine the effects of anti-angiogenic drugs on treatment efficacy using mathematically simulated data. For the first time, to the authors' best knowledge, computational modeling based on governing equations was employed before employing an ML method in order to prepare the dataset from the tumor growth simulation.

From an application perspective, this research also aimed to determine the most effective anti-angiogenic drug among bevacizumab, brolucizumab, and ranibizumab. Accordingly, the three ML methods determined the optimal chemotherapy administration time and concentration. A comparative analysis of the different ML algorithms was performed to determine the optimum prediction speed and accuracy. By classifying the cancer volume into three stages (day 30–40, 40–50, and 50–60), the effects of chemotherapy were monitored during different treatments. The integrative approach developed in this research, shown schematically in Fig. 1, is particularly effective for computationally intensive datasets, particularly when the dimensionality of the data exceeds the sample size, which is often the case in medical applications because of the limited availability of data. In addition to predicting the exact tumor volume and drug concentration required during tumor growth, this approach and its output can benefit oncologists in the administration of chemotherapy in actual practice for cancer treatment in the future.

Mathematic-based 3D modeling of tumor growth and its angiogenic network discretized the governing equations described in the methodology section. The centerpiece concept behind tumor growth simulation is the pressure gradient of the primary tumor cells, which grows under specific circumstances. After the simulation was completed, the collected dataset was imported into the ML algorithms for training. Subsequently, the three algorithms were evaluated according to different factors to determine the most accurate method in terms of prediction.

2. Methods

2.1. Simulation algorithm

The goal of the mathematical simulation model is to evaluate information about each step of tumor growth, measure how a drug can affect the tumor at different levels of growth, and predict its future status [80,81]. A recently developed mathematical simulation model was implemented using a programming language. In this study, the Hayato Yanagisawa model was modified for the simulation with some differences [21]. However, this study neglected the effects of angiopoietin on vessel growth. A step-by-step flowchart of the multiscale mathematical modeling of tumor growth developed in this study is presented in Fig. 2. Generally, tumor growth is divided into three different layers: cellular, intratumoral, and tissue level and the proposed model uses the pressure gradient as the basis for initiating tumor growth and further at the tissue level. The intratumoral level includes the mass transfer emitted from the

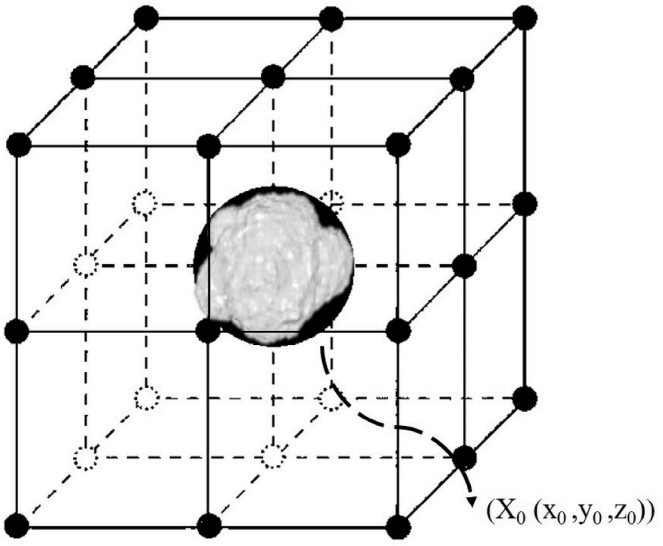

Fig. 4. The location of a tumor in three-dimensional space.

cell or transferred to it. This transfer consists of the TAF, nutrients, waste, and drugs. The computational model characterizes tumor growth physically and chemically from the avascular to the vascular state. It can also capture the destructive effects that remain in the tumor from different drug types and concentrations during angiogenesis.

At the tissue level, the tumor pressure model was used to examine the effect of pressure on neoangiogenesis and rapid cell division. The pressure of the avascular tumor, which leads to compression of the interstitial fluid of the endothelial cells and the rapid division of cells, named cell-induced tumor pressure (CTP), is observed at this stage [82–84]. Furthermore, vasculature-induced tumor pressure (VTP) is calculated when neovascularization caused by vessel perfusion occurs. The growth pressurization model uses CTP and VTP to calculate the total tumor pressure at the tissue level. At the beginning of the intratumoral level, the interstitial fluid velocity was calculated to investigate the transport of the tumor cell metabolism, drugs, and tumor angiogenesis factor (TAF) [85,86]. The distribution of each tumor growth factor, such as nutrients and waste obtained from cellular metabolism, TAF, and anti-angiogenesis drugs, is described by utilizing the discretization method to solve a set of partial differential equations numerically. Cell activity and cell vital energy (CVE) were determined to investigate cell phenotypes at the cellular level. Three different cell types were introduced: living, quiescent and necrotic cells. The proliferation process begins with cell division and tumor growth in living cells. The structure of this model is illustrated in Fig. 2 and it is clarified on Fig. 3.

In Fig. 2, all parameters are defined in a flowchart that can effectively simulate tumor growth progression from avascular to vascular states in the presence of the three drugs and concentrations.

The simulation started with five commonly planted endothelial cells in the center of a three-dimensional 1 cm3 space with 200 grid cells on each cube's surface. Each tumor cell resembles a sphere with a 60-μm diameter. Parent vessels are initially added as a stable input and grow as a dynamic vessel network during the following days. Drug treatment was initiated on day 40 of tumor growth stimulation, and its responses were investigated over the next 20 days.

2.2. Governing equations of tumor growth in different steps

The mathematical modeling was inspired by Yanagisawa's research, where the angiopoietin factor is considered and analyzed. However, this factor was neglected in this research because the aim was to find the best drug for an arbitrary simulated tumor. In the present model, two different definitions of tumor pressure were used by combining the CTP and VTP at a particular point which is the tumor location in a computational 3-D space X_0 (x_0,y_0,z_0) where CTP at X_0 is the summation of pressure across N tumor cells (Eq. (1)) [16]. Fig. 4 shows the location of a tumor cell in a three-dimensional (3D) space.

This tumor angiogenesis simulation was conducted for 60 days with half an hour of steps per day. Initial assumptions included O2 and VEGF factor uniformly diffused throughout the space, sufficient nutrients present, and blood vessels in a stable state.

The assumptions were as follows:

3. Tumor pressure, $p_0 = 60$ [mmHg] and capillary pressure, $p_V = 30$ [mmHg].
4. Tumors grow toward the lower interstitial pressure of 26 neighboring grid points.
5. Tumor migration is neglected in this simulation.

New sprouts occur when the condition of VEGF concentration equation is satisfied.

$$P^c X_0 = \sum_{i=1}^{N} (X_0.X_i) \tag{1}$$

$$N=(2k+1)^3 \tag{2}$$

In Eq. (1), P^c represents the pressure exerted by surrounding tumor cells at X_0. Hence, the number of these surrounding tumor cells is presented by Eq. (2) (mathematical based equation), where k is the number of grid points per side. Furthermore, P^c is the tumor pressure in X_i exerted on X_0. By knowing that the tumor pressure is determined by adding VTP value to CTP, VTP is defined as follows [20]:

$$P^v X_0 = \sum_{i=1}^{N} (X_0.X_i) \tag{3}$$

VTP is the sum of vascular endothelial cells that exist next to X_0. This means that VTP is considered only in the vascularized state of the tumor. Furthermore, the tumor pressure was assumed to be 60 mmHg, and the capillary pressure was 30 mmHg [21].

Oxygen is the essential nutrient necessary for tumor growth. The four different methods for oxygen transfer in a tumor are 1) diffusion, 2) convection, 3) secretion from blood cells, and 4) consumption by the tumor, which appear as vital terms in Eq. (4). Each partial differential equation (PDE) was solved using the finite difference method as part of the mathematical modeling. The following equation represents the tumor oxygen concentration [21]:

$$\frac{\partial o}{\partial t} = D_o \nabla^2 o - \nabla \cdot (u \cdot o) + \rho_o (r_v.(pv - p)) \delta_{\sum_v} - \lambda_o (A_i) \delta_{\sum_T} \tag{4}$$

where o is the tumor oxygen concentration mol.m^{-3}, D_o is the oxygen diffusion coefficient, p is the gradient of the tumor pressure, r_v is the removal term, and A_i is the activity of the tumor cells. These activities were related to the intratumoral layer in Fig. 2. In addition, $\delta_{\sum_v}$ indicates that oxygen secretion occurs only in vascular cells, but $\delta_{\sum_T}$ indicates that oxygen consumption is in all tumor cells. The oxygen secretion from blood cells is defined as follows [13].

$$\rho_o (r_v.(pv - p)) \delta_{\sum_v} = \rho_{n0} R_i W \tag{5}$$

In which ρ_{n0} is the oxygen supply rate, R_i is the vital nearest vessel radius, and W is the normalized weight function defined as Eq. (6) [20].

$$W = \frac{p_v - p}{p} \tag{6}$$

$$p_v - p \leq 0$$

Table 2
Different A_i values and cell status.

Cell status	Living cells	Quiescent cells	Necrotic cells
A_i	$A_i \geq 0$	$A_i = 0$	$A_i < 0$

Table 3
Parameter values for the 3D tumor model.

Symbol	Value	Unit	Description	Reference
Do	6.86	m^2/s	Oxygen diffusion coefficient	Estimated
ρ_{nO}	361025	ml/(cm^3s)	Oxygen supply rate	Estimated
λ_O	361025	ml/(cm^3s)	Oxygen consumption rate	Estimated
D_w	4610214	m^2/s	Carbon dioxide diffusion coefficient	Estimated
ρ_w	161025	mol/(m^3s)	Carbon dioxide secretion rate	Estimated
λ_w	2.56	ml/(cm^3s)	Carbon dioxide consumption rate	Estimated
Dc	1.26	m^2/s	VEGF diffusion coefficient	Estimated
ρ_C	261029	mol/(m^3s)	VEGF secretion rate	Estimated
λ_C	0	ml/(cm^3s)	VEGF consumption rate	Estimated
$Z1_d$	1.56	m^2/s	Bevacizumab diffusion coefficient	[87]
ρ_{Z1}	0.4	ml/(cm^3s)	Bevacizumab consumption rate	[87]
λ_{Z1}	0.088	ml/(cm^3s)	Bevacizumab decay rate	[87]
$Z2_d$	2.08	m^2/s	Ranibizumab diffusion coefficient	[87]
ρ_{Z2}	0.3	ml/(cm^3s)	Ranibizumab consumption rate	[87]
λ_{Z2}	0.052	ml/(cm^3s)	Ranibizumab decay rate	[87]
$Z3_d$	2.43	m^2/s	Brolucizumab diffusion coefficient	[88]
ρ_{Z3}	0.27	ml/(cm^3s)	Brolucizumab consumption rate	[88]
λ_{Z3}	0.048	ml/(cm^3s)	Brolucizumab decay rate	[88]
K_{active}	1	–	Rate of CVE addition by active cells	Estimated
$K_{quiescent}$	0.1	–	Rate of CVE addition by quiescent cells	Estimated
Ri	2	mm	Vessel radius	Estimated
K_{AR1}	1	–	Vessel radius constant	Estimated
K_{AR2}	500	–	Vessel radius constant	Estimated
p_i	0.26	mmHg	Osmotic pressure of interstitial fluid	Estimated
p_v	30	mmHg	Capillary/vascular pressure	[89]
p_c	60	mmHg	Tumor pressure	[89]
d_V	1	mol/m^3	Interstitial drug concentration	Estimated
n_0	8.4	mol/m^3	Standard nutrient concentration	Estimated
w_0	10.5	mol/m^3	Standard waste concentration	Estimated
C_0	4.36	kg/m^3	Standard VEGF concentration	[89]
D_o	2.13	mol/m^3	Standard drug concentration	Estimated

Table 4
Dataset distribution of AI algorithm which exists for different essential parameters.

Type of parameters	Parameter	Cell number		
Gradient	nutrient	8120601	6496481	1624120
	pressure	8120601	6496481	1624120
	drug	8120601	6496481	1624120
	waste	8120601	6496481	1624120
Tumor	activen number	1981	1584	397
	quiescent number	1981	1584	397
	necrosis number	1981	1584	397
Angiogenesis	vessel length	8120601	6496481	1624120
	TAF	8120601	6496481	1624120

where p_v is the vessel pressure, and p is the tumor pressure. If the tumor pressure is less than the arterial wall pressure related to the nearest vessel, oxygen secretion from the blood cells does not occur. Otherwise, it occurs when the arterial wall pressure exceeds the tumor pressure. For this purpose, the pressure weight function is used by Eq. (6) to represent the relative pressure during the tumor growth process [21].

The last term of the oxygen concentration PDE equation, Eq. (4), is related to the oxygen consumption by the tumor cell. Eq. (7) presents the different vital parameters [16].

$$\lambda_o(A_i) = \lambda_{o0} A_i \tag{7}$$

where λ_{o0} is the oxygen consumption rate, and A_i shows the activity of each tumor cell which is mentioned as the intratumoral layer in Fig. 3. This factor is measured by the amount of oxygen and carbon dioxide transferred in each cell. Eq. (8) is used in order to investigate this essential factor of tumor growth in terms of the cell state [21].

$$A_i = \frac{n}{n+1} \exp\left(-5(w-1)^4\right) \tag{8}$$

where w is the carbon dioxide concentration, another important cellular metabolic factor. This is modeled by the PDE equation in the same manner as the oxygen concentration rate equation with the same terms.

To understand the tumor cell's status, the A_i value should be considered to determine whether the cell is in a living, quiescent or necrotic state. Table 2 presents the cell status classifications for different A_i values [20].

In addition, cell vital energy (CVE) was introduced to measure the amount of energy stored in a cell for proliferation. In a living cell state (A_i»0), the cell activity stores energy for further proliferation, but in a quiescent state ($A_i = 0$), cells consume CVEs to support cellular life. The specific point in the CVE value, called the threshold level (t_{cve}), is a point for initiating the tumor cell proliferation process. Furthermore, for A_i «0, the cells were necrotic. CVE is presented by V_i, which depends on the cell activity (A_i) factor and k, which is related to the increasing CVE rate in two different living and quiescent states. The following equation presents this classification [16].

$$\frac{dv_i}{dt} \begin{cases} \frac{A_i}{A_i+1} K_{active} \cdot (active) \\ -\cdot K_{quiescent} \quad \text{(quiescent)} \end{cases} \tag{9}$$

The TAF factor measured the stimulation of blood vessels to cause capillary sprouting. The essential factor of TAF is VEGF, which is treated similarly in this model. As VEGF secretion causes angiogenesis in tumor cells, it is crucial to determine its concentration in each cell type. The following equation is a PDE that represents VEGF concentration by introducing different practical terms [20]:

$$\frac{\partial c}{\partial t} = D_c \nabla^2 c - \nabla \cdot (u \cdot c) + \rho_c (rv.(pv - p)) \delta_{\sum_v} - \lambda_c(A_i) \delta_{\sum_T} \tag{10}$$

where c is the VEGF concentration and D_c is its diffusion. ρ_c is a VEGF secretion rate and λ_c is its consumption rate, which means VEGF removal from the vessel. $\delta_{\sum_T}$ indicates the process in tip endothelial cells (TEC). These terms are described in the following equations [13]:

$$\rho_c(n) = \rho_{c0}(1-n) \tag{11}$$

$$\lambda_c(rv) = \lambda_{c0} R_i \tag{12}$$

$$R_i = \frac{Age_i}{Age_i + K_{AR2}} K_{AR1} \tag{13}$$

Eq. (11) presents the effective parameter of VEGF. where ρ_{c0}

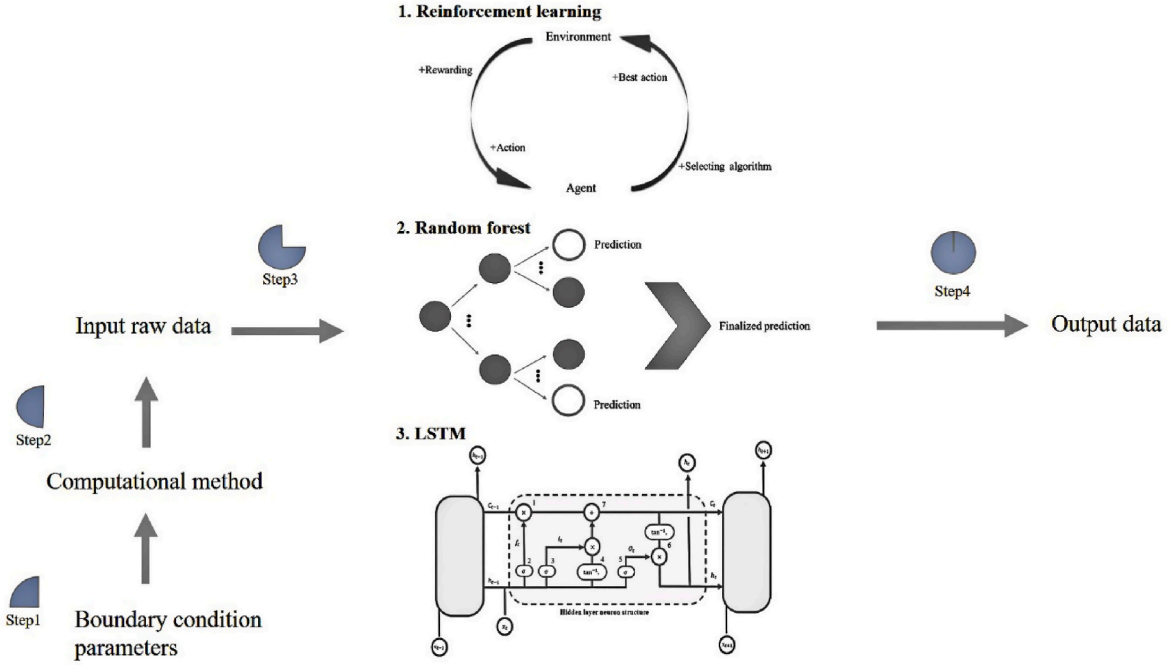

Fig. 5. Overall structural methodology of this study.

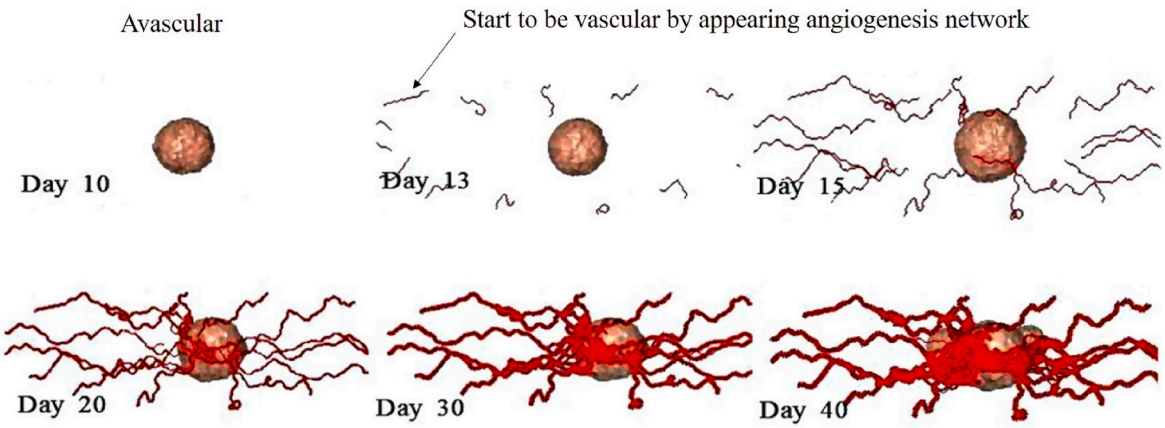

Fig. 6. Different tumor growth stages and morphologiacal variations in the tumor in the absence of anti-angiogenic drugs.

represents the VEGF secretion rate. On the one hand, R_i depends on time and increases with it. On the other hand, the nutrient delivery and waste removal from the cell rise too. In Eq. (13), Age_i presents the time for sprouting new vessels while K_{AR1} and K_{AR2} are constant values. These properties are obtained from Table 3. The other essential factors for cellular metabolism are carbon dioxide and waste concentration in a cell tumor. PDE models these with the same oxygen concentration relation. Critical topics while studying angiogenesis are the direction and speed of vessel extension. These directly depend on the VEGF factor because vessel extension occurs in regions of high hypoxia.

A chemotherapy method was used to prevent angiogenesis. This study chose three anti-angiogenic drugs to inhibit new blood vessel sprouting and bind to VEGF. A PDE can model drug concentration in a tumor cell with the same four main terms as an oxygen concentration (Eq. (4)) plus one additional term related to the decay term as follows: [21].

$$\frac{\partial Z}{\partial t} = D_Z \nabla^2 Z - \nabla \cdot (u \cdot Z) + \rho_Z (rv.(pv - p)) \delta_{\sum_v} - B - \lambda_z d \quad (14)$$

where Z indicates each drug among the three drugs (Bevacizumab, Ranibizumab, and Brolucizumab from Z1 to Z3 in Table 3). Also, in Eq. (14), D_z is the drug diffusion rate, ρ_Z is the consumption rate, λ_Z is a decay rate and B is the binding of a drug to VEGF. B is added to the main equation by considering the drug simulation performance.

2.3. Preparation of dataset for the ML algorithms

The datasets obtained from the mathematical simulation represent tumor growth and angiogenesis. For each timestep, 1 s in this research, a snapshot from a visualization of tumor growth and related data were collected in several vital parameters of the growth process (Table 4). To this end, nine different simulation runs (optimized between several runs from 1 to 11) were performed, each for 60 days from the first day of the avascular stage to the last tumor growth stage. Each step (in seconds) provided an image with unique features and information about the tumor stage, which was utilized to input the ML algorithms [90]. Each dataset contained three categories of different stages of the simulation. Table 4 presents the data distribution for different essential parameters,

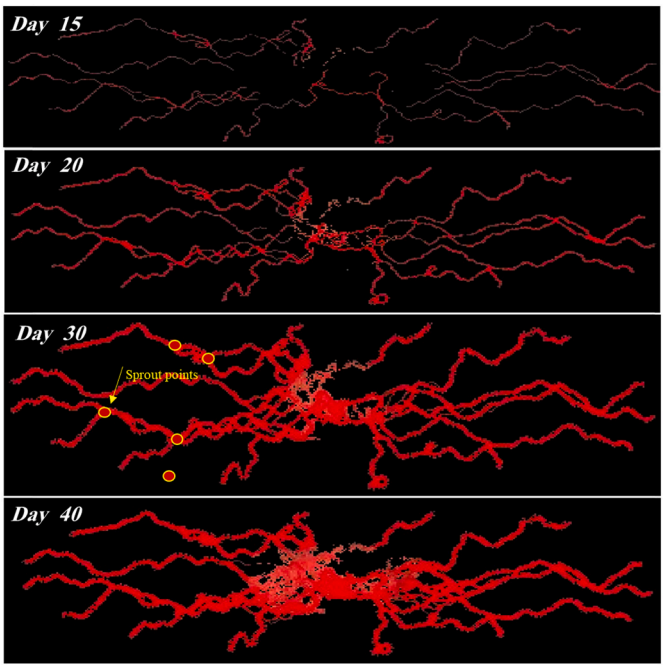

Fig. 7. VEGF concentration in a tumor in the presence of a microvascular network near cancer.

which were generalized for all nine different states (three drugs and three concentrations). The dataset was split to produce the training and testing datasets at a ratio of 9 1. In other words, 90% of the data were used for training and 10% for testing.

As shown in Table 4, each row presents a different vital parameter for tumor growth and the column named "cell number" means the total number of tumor cells at a cellular level. So, we have a related parameter for each cell status, e.g.(nutrient gradient, VEGF factor). So the contribution of this table in machine learning algorithms is to make a dataset from each cell status and then use it in the prediction modeling with AI.

The importance of the dataset size reflects on the learning accuracy. According to the ML requirement, the simulation should be developed to prepare a suitable dataset as an input for the ML algorithms. Although the trained algorithms will be reduced the overall calculation time, the simulation time still plays a vital role in dataset preparation. So the simulation time steps are considered half an hour during 50 days of simulation. So, there is suitable tumor data, and its visualization exists for each time step. Concerning these assumptions, the dataset contains 2400 time steps, and for each of them, the tumor growth information and its visualized images, the splitting rate for train and test datasets, 2160 data for training the ML algorithms, and 240 data for testing them. Furthermore, 50 arbitrary randomized data from 2400 data are used for the validation dataset. As one of the main goals of this study is to have a comparative analysis between different ML algorithms, it was decided to have the same splitting rate for three utilized algorithms.

2.4. Predictive modeling

The proposed prediction model aims to overcome the need for lengthy and computationally expensive simulation models. It can predict anti-angiogenic therapeutic effects on complex tissues, including the concentration of tumor growth and chemotherapy-related parameters, rate of increase in necrotic cells, and new vessel length. Moreover, the ability to collect this dataset from the mathematical simulation into a high-throughput format necessitates the generation and efficient handling of large datasets and utilizing ML methods to predict drug treatment effects on a tumor based on the simulation. Rapid predictive modeling is essential for monitoring and forecasting tumor growth and the effect of drug treatments because there is a lack of time from prediction to the start of anti-angiogenic therapy for each clinical trial case. Different steps visualization of tumor development before and after chemotherapy is the main goal, with ML methods potentially being able to increase the speed and accuracy of old computational simulations. As mentioned above, the primary input into the ML models was the output of the mathematical simulation, which was taken as the input at a given step in the total simulation time. Because of the nature of the parameters studied here, it was necessary to use two basic types of AI methods (supervised and RL), and each was evaluated and compared. In RL, the output is not independent of the state of the input in the current stage of learning, and the next stage output depends on the previous output. In supervised learning, the decision is made based on the current input. Moreover, it uses labeled datasets from this action, whereas in RL, the dataset comprises the data status and previous action. The agent of the RL is the computer. The action is to define how much the tumor grows in the experimental environment and compare doctor detection concerning artificial intelligence detection. Also the environment is a

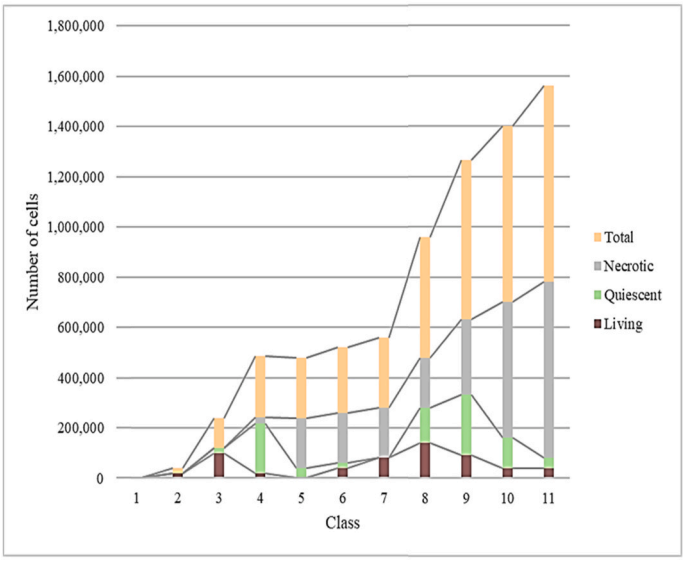

Class	Iteration
1	0
2	200
3	400
4	600
5	800
6	1000
7	1200
8	1400
9	1600
10	1800
11	1980

Fig. 8. The number of cells in each of the three different cell types during the simulation. The *x*-axis represents iteration numbers grouped into classes to aid visualization.

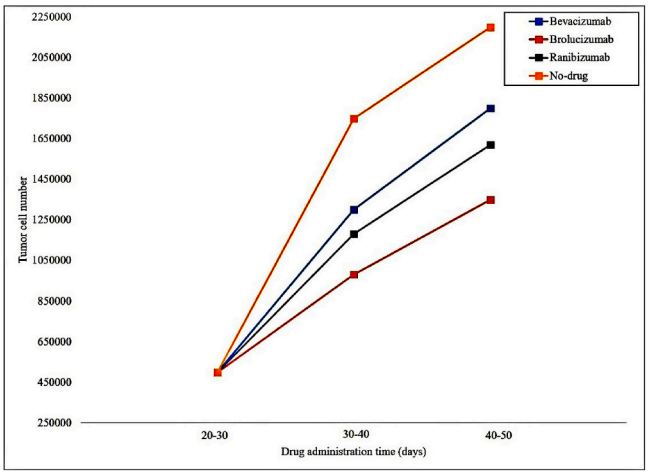

(a)

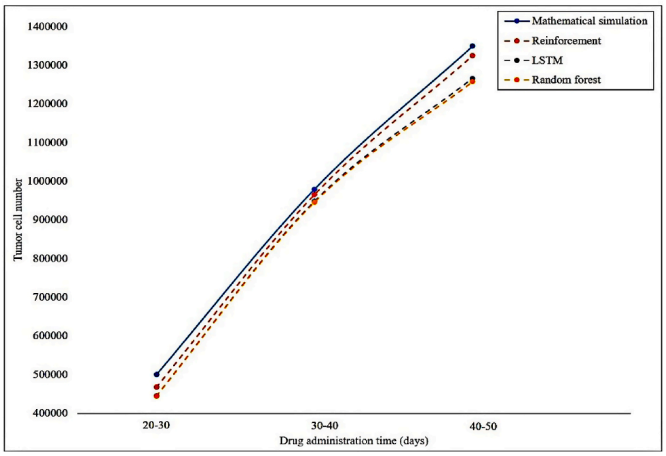

(b)

Fig. 9. The number of tumor cells in three-drug administration periods (days). (a) tumor cell number in a chemotherapy-treated situation with validation and (b) comparison between mathematical simulation and ML methods.

computational domain with described conditions (Fig. 5), and the state and the reward situation are related to the comparison between the doctor detection and trained algorithm detection. Fig. 5 shows the structural differences between supervised learning and RL. Three AI methods are considered after the feature extraction procedure. The methods utilized were RL, RF, and LSTM. The emergence of an AI method based on feature extraction through simulation outputs resulted from this research to analyze and investigate all related parameters owing to the mathematical simulation of a tumor. These methods provide a computational tool trained on simulation results and modeling images.

Seven different metrics were calculated to evaluate algorithm performance: MAE, RMSE, ACC, FPR, TPR, PPV and TNR. The definitions of these metrics are given in Eqs.(15)–(22) [91].

$$MAE = \frac{(real\ value - predicted\ value)}{real\ value} \tag{15}$$

$$RMSE = \sum_{i=1}^{n} \sqrt{\frac{(real\ value - predicted\ value)^2}{n}} \tag{16}$$

$$ACC = \frac{T_P + T_N}{T_P + T_N + F_P + F_N} \tag{17}$$

$$FPR = \frac{F_P}{T_N + F_P} \tag{18}$$

$$TPR = \frac{T_P}{T_P + F_N} \tag{19}$$

$$PPV = \frac{T_P}{T_P + F_P} \tag{20}$$

$$TNR = \frac{T_N}{T_N + F_P} \tag{21}$$

$$FNR = \frac{F_N}{T_P + F_N} \tag{22}$$

Real value introduces simulation results, and predicted value introduces the algorithm results, T_P is true positive, T_N is true negative, F_P is false positive, and F_N is false negative [91].

As presented in Fig. 5, the proposed method of this study is presented in different steps.

Step 1 Consider a 3-dimensional cube where the primary endothelial cell exists in the middle of the assumed cube. Define suitable boundary conditions and essential parameters for arbitrary endothelial cells to initialize the governing equations of tumor growth and angiogenesis.

Step 2 The finite element method describes these equations based on the transport phenomenon. This procedure was implemented using commercial software. Eleven runs were undertaken to determine the most accurate approach compared to Yangisawa's study. Moreover, each run involved several iterations, leading to convergence. The compiling procedure aims to compute critical factors vital for tumor growth, such as nutrient VEGF and oxygen concentration.

Furthermore, drug concentrations were computed. Three anti-angiogenic drugs were tested in this study. The most effective method for preventing tumor growth by reducing angiogenesis has been introduced.

Step 3 Data collected from the computational model were used as inputs for the ML algorithms. Three different ML algorithms are studied separately in order to find the most accurate one in the case of predicting modeling.

The main aim of this study was to select the best ML algorithm for predicting tumor state at an arbitrary moment of the chemotherapy treatment procedure. Therefore, a comparative analysis was performed to determine the most accurate method.

Step 4 Finalize the most accurate algorithm by evaluating different evaluation factors

3. Results and discussion

3.1. Angiogenesis modeling during tumor growth

VEGF plays a vital role in physiological angiogenesis, a characteristic of tumor growth, and is secreted by hypoxia in tumors. Excessive secretion of VEGF and an increase in its concentration leads to tumor angiogenesis and expands the microvascular network [92]. Given the high clinical importance of VEGF and visualizing the capillary network around the tumor (shown in Fig. 5), the VEGF concentration at each stage should be determined using computational methods. It was investigated because of their obvious concentrations in different tumour regions. Fig. 6 presents the VEGF concentration in the vessels was

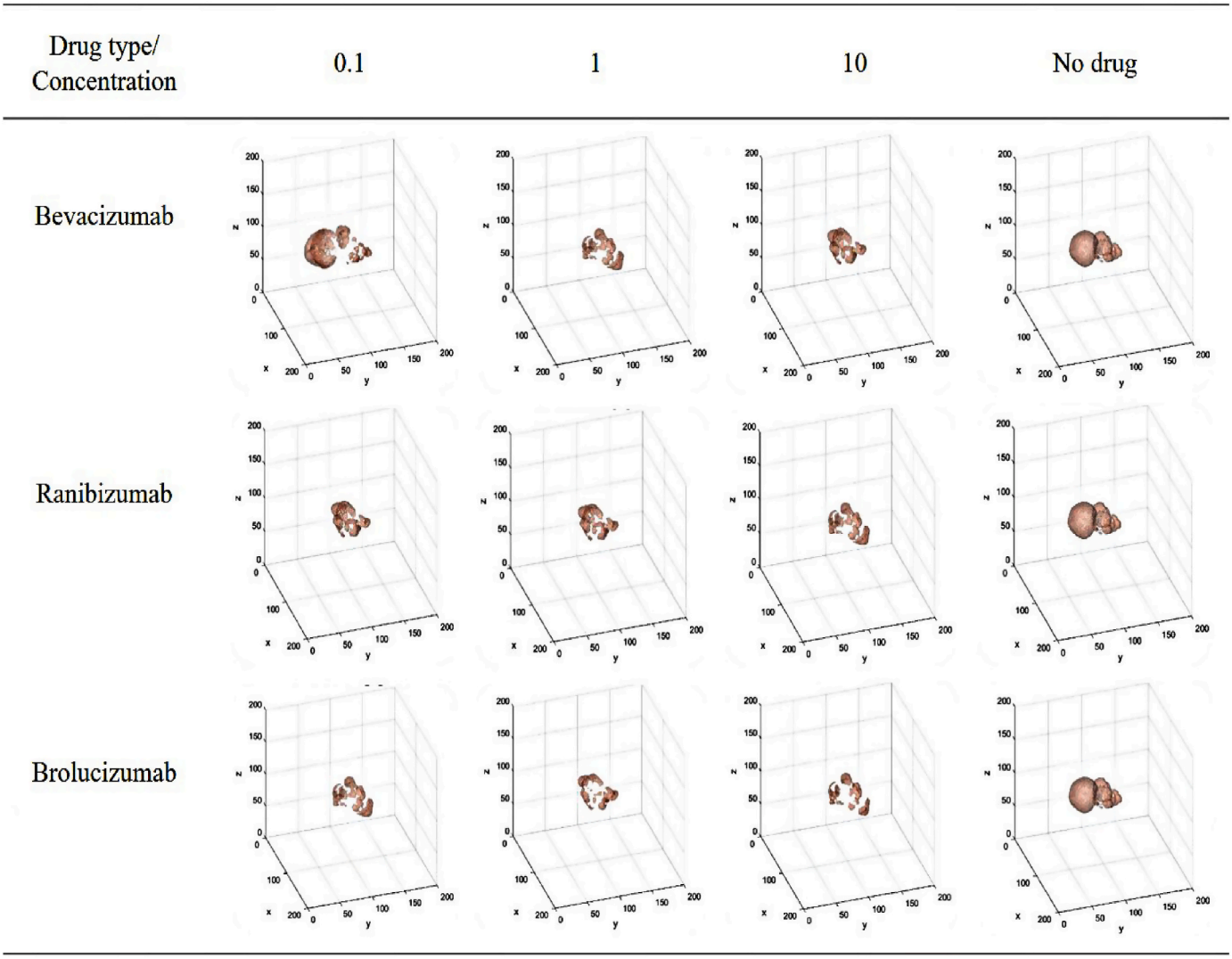

Fig. 10. The effect of different drugs and concentrations on the 60th day of simulation.

determined from the day of neoangiogenesis starting on the day of the chemotherapy drugs reaching the tumor.

3.2. Radiomic features extraction for tumors (VEGF)

As presented in Fig. 6, the characterization of the tumor growth process involves two distinct stages: avascular and vascular. The first stage occurs during protein synthesis and proliferation of tumor cells when the tumor size is approximately 1–3 mm [92]. As hypoxia occurs, uncontrolled proliferation appears in a cell, and the tumor enters the vascular stage [93]. The initialization of angiogenesis at the vascular stage in the second stage creates a new supply rate of nutrients for further tumor growth. Fig. 7 presents the different tumor growth stages and morphological variations of the tumor without anti-angiogenic drugs.

VEGF concentrations during the different tumor growth stages are shown in Fig. 7. Tumor cells secrete VEGF to expand their vascular networks and increase their proliferation rate. The VEGF concentration in the microvessels around the tumor is shown in red in Fig. 6, with thicker dots indicating higher concentrations and lower concentrations of lighter dots. In addition, the number of sprouting points around the tumor increased during the subsequent growth steps. These points form from each vessel and increase in number, and the length of these vessels can also increase [94–96]. A 3D model encompassing both angiogenesis and tumor growth is shown in Supplementary Video 1.

Supplementary video related to this article can be found at https://doi.org/10.1016/j.compbiomed.2022.105511

3.3. Therapeutic effects of anti-angiogenic drugs on tumor growth

Three anti-angiogenic drugs used to prevent abnormal increases in VEGF concentrations in tumor cells were investigated to evaluate their impact on treatment outcomes. The treatment results were followed for 20 days, from 40 to 60 days post-injection. One of the criteria in which the effects of a drug on tumor cells are well observed is the number of living, quiescent and necrotic cells. These states were used to determine the status of the cells during treatment. Living cells refer to cells with regular activity in a tumor, quiescent cells refer to inactive cells that cannot produce more cells, and necrotic cells refer to dead cells. During the simulation, the iteration steps (each iteration involved solving the governing equations) were divided into 11 classes (shown on the right-hand side of Fig. 8). Fig. 8 shows the number of cells in these three groups across the 11 classes.

Each bar in Fig. 8 represents a specific class of iterations in the mathematical simulation. As shown, the number of living cells in the tumor initially increases. Subsequently (e.g., class 4), by adding chemotherapy treatments, they decreased, whereas the numbers of quiescent and necrotic cells increased with iteration. Chemotherapy

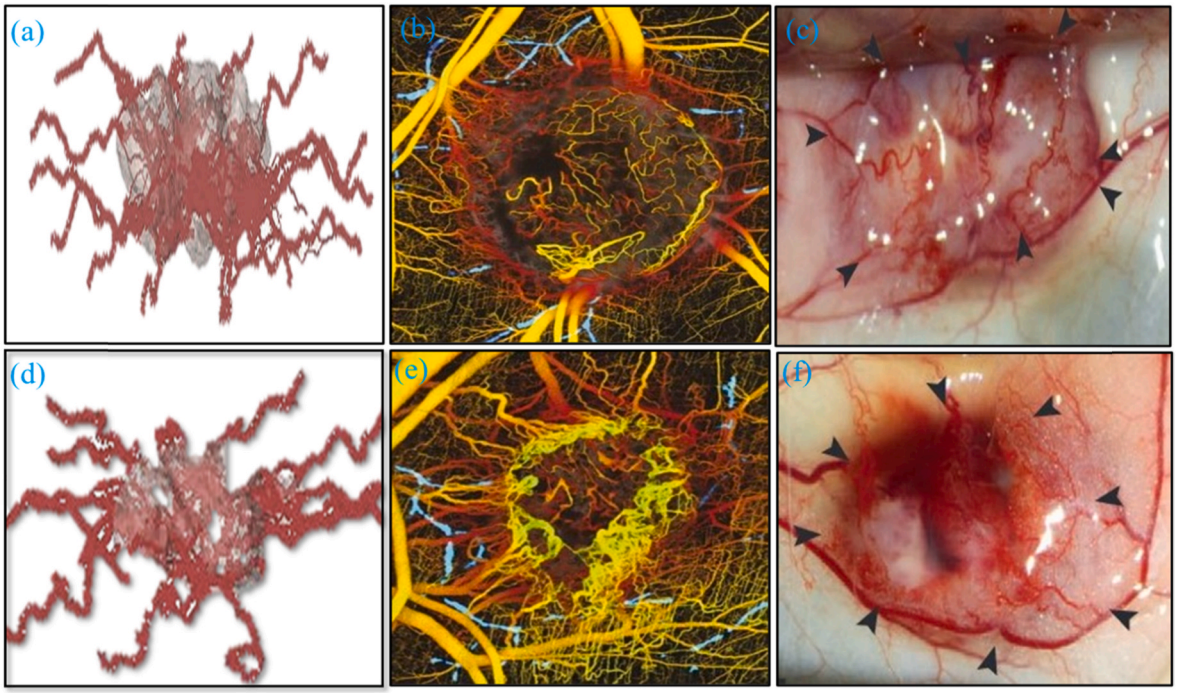

Fig. 11. Validation between this study and two different studies. The first column presents a recent tumor growth model. (a) shows the 40th day of the simulation, the last day before starting chemotherapy drug treatment, and (d) presents the five days after treatment (day:45). Also the second column presents optical frequency domain imaging (OFDI), and the last one presents microscopic imaging of a tumor as a clinical study, respectively. Each row presents the same time in a tumor growth procedure.

reverses the increasing trend in the number of living cells by converting them into quiescent and necrotic cells. This process continues until the endothelial cells are completely replaced with necrotic cells.

Another approach to highlighting anti-angiogenic drugs' effects on tumor growth is to investigate the significant differences between treatment outcomes of the no-drug state and the three anti-angiogenic drug groups after 60 days, as shown in Fig. 8. For the bevacizumab-treated tumor, the number of tumor cells was significantly decreased than that in the brolucizumab-treated tumor. As shown in Fig. 9, three different drug administration periods were selected: (*i*) 20–30 days, (*ii*) 30–40 days, and (*iii*) 40–50 days. In the 40–50 day class, the relative increase in the number of tumor cells in a Ranibizumab-treated tumor was significantly smaller than that in a brolucizumab-treated tumor, although no significant difference was observed in the 20–30 class, as the tumor is constantly growing without any treatments in this period. In contrast, tumor cell numbers in both Ranibizumab and Brolucizumab-treated tumors in the no-drug group were significantly increased in the 40–50 class (see Fig. 9).

Fig. 9(a) shows that brolucizumab was the most effective drug among the three investigated drugs. This drug decreases the tumor cell number by 44% in the period 30–40 days and 39% in the period 40–50 days. Fig. 9(b) presents the predictions of the tumor cell numbers obtained using the three different AI methods. Such a prediction could help determine the number of tumor cells at a specific time during treatment and follow-up on the efficacy of chemotherapy drugs. A comparative analysis was performed in Fig. 9(b) to determine the most accurate AI algorithm. The most precise method was reinforcement learning with a 1.8% mean absolute error (MAE).

To analyze the effect of chemotherapy in reducing the number of tumor cells, it is necessary to investigate the status of the no-drug group. By initiating the tumor visualization method (starting with a specific diameter of a sphere as an initial tumor cell) with some described conditions as it is shown in Figs. 4 and 10 presents the developed model of a tumor considering the effect of the three different drugs as well as their concentrations on a simulated tumor on the 60th day of the simulation. The efficacy of these drugs for solid tumor treatment is shown in Supplementary Video 2.

Supplementary video related to this article can be found at https://doi.org/10.1016/j.compbiomed.2022.105511

As presented in Fig. 10, the smallest remaining volume belongs to Brolucizumab with 10 $\frac{mol}{m^3}$ concentration and the largest one to Brolucizumab with 0.1 $\frac{mol}{m^3}$ Concentration. The number of necrotic and quiescent tumor cells should be subtracted from the total number of cells to determine the number of living cells. Furthermore, this procedure is validated with an experimental study on a mouse and another study [97, 98]. Fig. 11 presents this validation compared with this study and another one.

The final volume of the simulated tumor with nine different treatment states (i.e., three different concentrations of three different drugs) was calculated and presented in Fig. 12. The percentage effectiveness of each drug is shown in Table 5.

In Fig. 12(a), necrotic and quiescent cells were subtracted from the total number of tumor cells, and only living cells were shown. In addition, Fig. 12(b) compares the mathematical simulation results and predictions using the three different AI methods for the brolucizumab. Reinforcement learning was the best AI method, with an average MAE value of 2.7%.

As presented in Table 5, the percentage effectiveness of brolucizumab in the two different periods was the largest among the three drugs, with bevacizumab being the smallest. It can be concluded from the mathematical simulation that the most effective drug against tumor growth is brolucizumab.

3.4. Drug administration period and tumor growth

To determine the most effective time for tumor growth inhibition, three different treatments were applied at three different administration periods: (*i*) 30–40 days, (*ii*) 30–50 days, and (*iii*) 30–60 days, within a 60-day simulation period. The effects of the treatment on the new vessel length for each drug are presented in Fig. 13. Moreover, the validity of

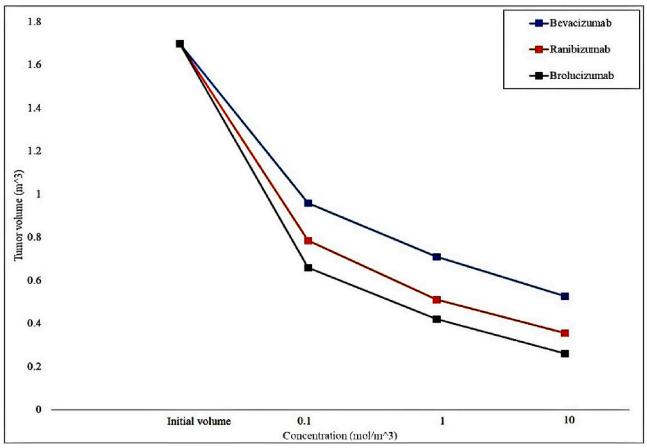

(a)

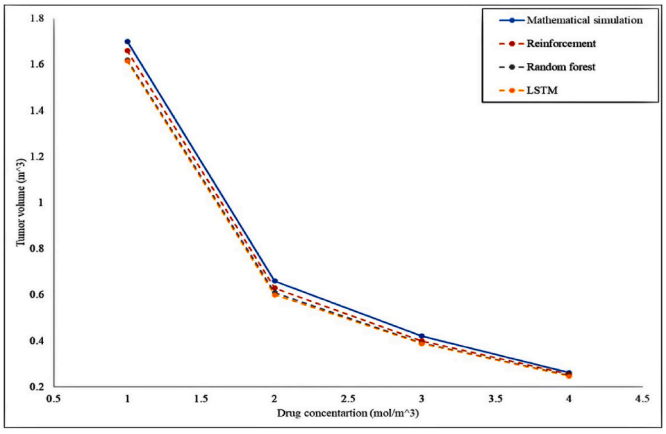

(b)

Fig. 12. Total tumor volume on the 60th day of simulation. (a) Variation in tumor volume with three different anti-angiogenic drugs; (b) comparison between mathematical simulation results and predictions with varying methods of AI for the drug brolucizumab.

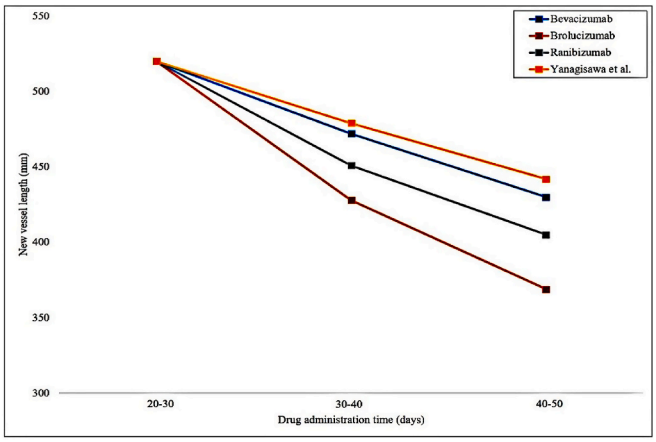

(a)

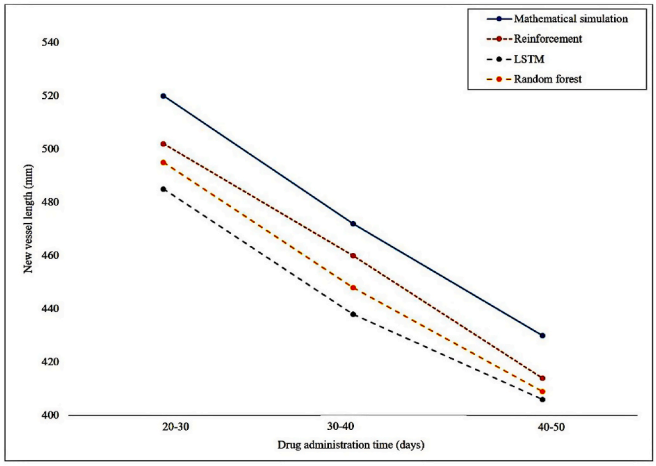

(b)

Fig. 13. The effect of treatment on the length of new vessels for all drugs. (a) Comparison of new vessel length for different medicines and previously-published study. (b) Efficacy of different AI methods compared to simulated data.

Table 5
The percentage effectiveness of each chemotherapy drug.

Classification (days)	Effectiveness (%)		
	Bevacizumab	Ranibizumab	Brolucizumab
40–50	25.4	26.3	31.2
50–60	26.5	28.2	42.2

the proposed mathematical simulation is compared to that of Yanagisawa's simulation [21].

Fig. 13(a) shows that the minimum vessel length in the 30–60 day period was obtained for brolucizumab-treated tumors. In contrast, the maximum total length of new vessels was obtained for bevacizumab-treated tumors. On the other hand, the maximum vessel length was achieved for the 30–40 days when no drug was used to treat the tumor. By comparing the present study with Yanagisawa's study [21], it can be concluded that the new vessel length was reduced by 16% with brolucizumab. Fig. 13(b) shows a comparative analysis of the three AI methods. The most accurate method was RL, with an average MAE of 3.7%.

3.5. Statistical analysis for evaluating model performance

Three commonly used AI algorithms for estimating tumor growth parameters (length of new capillaries, number of tumor cells, and tumor volume) were assessed, and the model performances are reported in Table 6.

Statistical analysis was performed and assessed using MAE, root mean square error (RMSE), accuracy (ACC), specificity (FPR), sensitivity (TPR), positive predicted values (PPV), and true negative rate (TNR). Based on the investigation results, the highest accuracy was achieved by RL, with an MAE value of 0.033 and an accuracy of 0.943 on average. Furthermore, ROC curves of different values related to each parameter are shown in Fig. 14. Also, the confusion matrix is presented in Fig. 15, respectively.

4. Conclusion

This study used a 3D simulation of tumor growth and its dynamic microvascular network to investigate the efficacy of three different anti-angiogenic drug treatments. Based on the simulation results, increasing the drug concentration from 0.1 to 10 $\frac{mol}{m^3}$ increased the rate of living cells replaced by necrotic cells. The results demonstrated that brolucizumab is the most effective anti-angiogenic drug among the three investigated drugs at 50-60th days.

The results show that the tumor volume decreases with different anti-angiogenic drugs, but it is also affected directly by the drug concentration. The TAF factor was reduced by applying anti-angiogenic

Table 6
Performance evaluation of different AI algorithms for estimating tumor growth parameters.

Parameter	Method	TNR	PPV	TPR	FPR	ACC	RMSE	MAE
New vessel length (mm)	Reinforcement	0.950	0.951	0.924	0.050	0.937	15.535	0.032
	LSTM	0.927	0.930	0.903	0.073	0.915	16.422	0.064
	Random forest	0.913	0.918	0.874	0.087	0.892	31.984	0.067
Tumor cell number	Reinforcement	0.960	0.961	0.933	0.040	0.946	24.885	0.032
	LSTM	0.978	0.979	0.913	0.022	0.944	37.523	0.068
	Random forest	0.966	0.969	0.896	0.034	0.928	51.542	0.071
Tumor volume (m^3)	Reinforcement	0.951	0.950	0.941	0.049	0.946	27.586	0.036
	LSTM	0.989	0.990	0.924	0.011	0.954	25.887	0.061
	Random forest	0.978	0.980	0.901	0.022	0.937	16.225	0.069

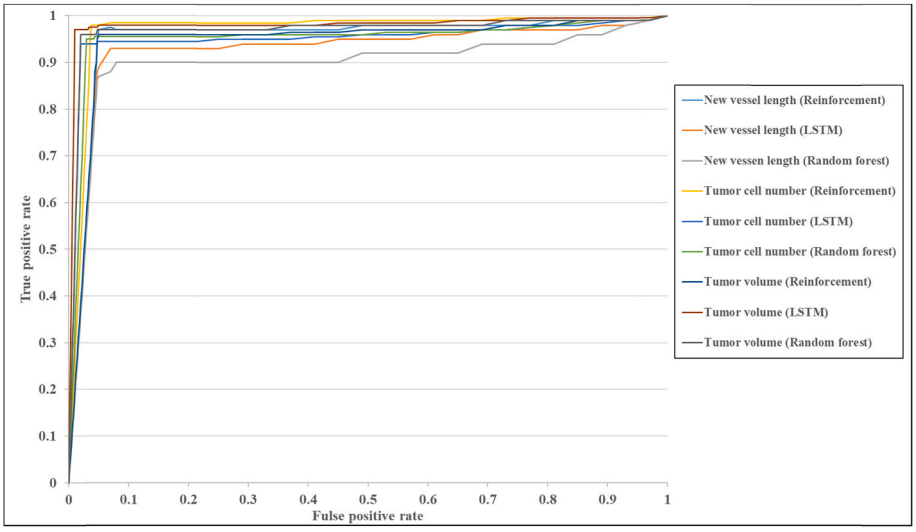

Fig. 14. ROC curve of different ML algorithms are presented for each tumor growth vital parameter.

Fig. 15. Confusion matrix of different ML algorithms are presented for each tumor growth vital parameter.

drugs (based on tumor volume), leading to a decreased tumor volume in the rest of the simulation. Another critical effect of drugs on tumor structure is a decrease in the length of new vessels that appear naturally near the tumor and sprout to areas that suffer from lack of oxygen. The rate of decline in the length of new vessels is up to 16% compared to that in Ref. [21] with brolucizumab. Furthermore, brolucizumab reduced the number of tumor cells by 44% in the 30–40 day period and 39% in the 40–50 day period, demonstrating that anti-angiogenic drugs could respond directly to tumor vessel length during the 40–60 day period. Through AI learning, it was possible to predict various tumor properties at all stages of tumor growth, potentially increasing the speed of detection given the drug treatment. By employing AI methods, the tumor characteristics can be known by clinicians at any time. The efficacy of different drug treatments can be evaluated before starting a treatment or any time afterward.

To increase the accuracy of the simulation methods and the prediction speed, it is critical to use the most up-to-date AI methods. Three different AI learning methods were used in this study (RL, RF and LSTM). According to the results of the comparative analysis between different algorithms, the most powerful method for predicting tumor cell count properties was RL, with a mean absolute error of 3.33% and accuracy of 94.3%. This research demonstrates the utility of AI methods for predicting tumor growth and properties as a fast alternative to computationally expensive (and slow) tumor growth simulations. To be more clarified, supercomputers should solve these equations related to the sophisticated equations of the tumor growth that should be coupled during simulation to consider all of the vital parameters to model this procedure. These computers are so expensive and need time to do these mathematical calculations. Hence, it has the benefit of interpolating between different simulation outcomes, allowing clinicians to access real-time information on drug efficacy at the time of treatment and, subsequently, at further intervention periods. Using the presented approach of employing AI algorithms immediately after the mathematical simulation, computational costs were reduced, and the speed and accuracy of calculations increased. The investigated AI modeling approach can help clinicians by providing more accurate predictions of tumor post-treatment and supporting more beneficial treatment plans for patients. The accuracy and the performance of the proposed models can be improved through further research and conducting comparative analysis involving the hybrid machine learning and deep learning methods trained with the aid of advanced optimization methods, e.g., Refs. [99–104]. Future research can be devoted to finding the optimal configuration of machine learning and evolutionary methods for an optimal training for a particular modeling application.

Funding

Project no. 2019–1.3.1-KK-2019-00007 was implemented with support from the National Research, Development and Innovation Fund of Hungary, financed under the 2019–1.2.1-KK funding scheme. LK was supported by the Eötvös Lóránd Research Network Secretariat under grant agreement no. ELKH KÖ-40-2020 (Development of cyber-medical systems based on AI and hybrid cloud methods). AM was suported by funding from the European Union's Horizon 2020 Research and Innovation Programme under the Programme SASPRO 2 COFUND Marie Sklodowska-Curie grant agreement No. 945478.

Informed consent statement

No human or animal materials had been used in this research.

Data availability statement

The data are available from the first author on reasonable request.

Declaration of competing interest

Authors declare no conflict of interests.

References

[1] S. Jafari Nivlouei, M. Soltani, J. Carvalho, R. Travasso, M.R. Salimpour, E. Shirani, Multiscale modeling of tumor growth and angiogenesis: evaluation of tumor-targeted therapy, PLoS Comput. Biol. 17 (6) (2021 Jun 23), e1009081.
[2] D. Ribatti, F. Pezzella, Overview on the different patterns of tumor vascularization, Cells 10 (3) (2021 Mar) 639.
[3] W. Olejarz, G. Kubiak-Tomaszewska, A. Chrzanowska, T. Lorenc, Exosomes in angiogenesis and anti-angiogenic therapy in cancers, Int. J. Mol. Sci. 21 (16) (2020 Jan) 5840.
[4] C.R. Park, J.S. Lee, C.G. Son, N.H. Lee, A survey of herbal medicines as tumor microenvironment-modulating agents, Phytother Res. 35 (1) (2021 Jan) 78–94.
[5] S. Dikici, A.J. Bullock, M. Yar, F. Claeyssens, S. MacNeil, 2-deoxy-d-ribose (2dDR) upregulates vascular endothelial growth factor (VEGF) and stimulates angiogenesis, Microvasc. Res. 131 (2020 Sep 1), 104035.
[6] A. González-González, A. González, N. Rueda, C. Alonso-González, J. M. Menéndez, C. Martínez-Campa, S. Mitola, S. Cos, Usefulness of melatonin as complementary to chemotherapeutic agents at different stages of the angiogenic process, Sci. Rep. 10 (1) (2020 Mar 16) 1–20.
[7] F. Guo, J. Cui, Anti-angiogenesis: opening a new window for immunotherapy, Life Sci. (2020 Jul 29), 118163.
[8] R.I. Teleanu, C. Chircov, A.M. Grumezescu, D.M. Teleanu, Tumor angiogenesis and anti-angiogenic strategies for cancer treatment, J. Clin. Med. 9 (1) (2020 Jan) 84.
[9] O.T. Inan, P. Tenaerts, S.A. Prindiville, H.R. Reynolds, D.S. Dizon, K. Cooper-Arnold, M. Turakhia, M.J. Pletcher, K.L. Preston, H.M. Krumholz, B.M. Marlin, Digitizing clinical trials, NPJ Digital Med. 3 (1) (2020 Jul 31) 1–7.
[10] A.S. Choudhari, P.C. Mandave, M. Deshpande, P. Ranjekar, O. Prakash, Phytochemicals in cancer treatment: from preclinical studies to clinical practice, Front. Pharmacol. 10 (2020 Jan 28) 1614.
[11] M. Soltani, P. Chen, Numerical modeling of interstitial fluid flow coupled with blood flow through a remodeled solid tumor microvascular network, PLoS One 8 (6) (2013 Jun 26), e67025.
[12] Z. Wang, J.D. Butner, R. Kerketta, V. Cristini, T.S. Deisboeck, Simulating cancer growth with multiscale agent-based modeling, InSeminars Cancer Biol. 30 (2015 Feb 1) 70–78. Academic Press.
[13] L.A. Harris, S. Beik, P.M. Ozawa, L. Jimenez, A.M. Weaver, Modeling heterogeneous tumor growth dynamics and cell–cell interactions at single-cell and cell-population resolution, Curr. Opin. Struct. Biol. 17 (2019 Oct 1) 24–34.
[14] H. Bazmara, M. Soltani, M. Sefidgar, M. Bazargan, M. Mousavi Naeenian, A. Rahmim, The vital role of blood flow-induced proliferation and migration in capillary network formation in a multiscale model of angiogenesis, PLoS One 10 (6) (2015 Jun 5), e0128878.
[15] N. Zahir, R. Sun, D. Gallahan, R.A. Gatenby, C. Curtis, Characterizing the ecological and evolutionary dynamics of cancer, Nat. Genet. 52 (8) (2020 Aug) 759–767.
[16] G. Vilanova, I. Colominas, H. Gomez, Computational modeling of tumor-induced angiogenesis, Arch. Comput. Methods Eng. 24 (4) (2017 Nov) 1071–1102.
[17] M. Ahmadlou, H. Adeli, Complexity of weighted graph: a new technique to investigate structural complexity of brain activities with applications to aging and autism, Neurosci. Lett. 650 (2017) 103–108.
[18] J. delEtoile, H. Adeli, Graph theory and brain connectivity in Alzheimer's disease, Neuroscientist 23 (6) (2017) 616–626.
[19] M. Mozaffari Legha, H. Adeli, Visibility graph analysis of speech evoked auditory brainstem response in persistent developmental stuttering, Neurosci. Lett. 696 (2019) 28–32.
[20] L. Tang, A.L. Van De Ven, D. Guo, V. Andasari, V. Cristini, K.C. Li, X. Zhou, Computational modeling of 3D tumor growth and angiogenesis for chemotherapy evaluation, PLoS One 9 (1) (2014 Jan 3), e83962.
[21] H. Yanagisawa, M. Sugimoto, T. Miyashita, Mathematical simulation of tumour angiogenesis: angiopoietin balance is a key factor in vessel growth and regression, Sci. Rep. 11 (1) (2021 Jan 11) 1–3.
[22] T.T. Tang, J.A. Zawaski, K.N. Francis, A.A. Qutub, M.W. Gaber, Image-based classification of tumor type and growth rate using machine learning: a preclinical study, Sci. Rep. 9 (1) (2019 Aug 29), 1-0.
[23] L.B. Zwep, K.L. Duisters, M. Jansen, T. Guo, J.J. Meulman, P.J. Upadhyay, J. C. van Hasselt, Identification of high dimensional omics-derived predictors for tumor growth dynamics using machine learning and pharmacometric modeling, CPT Pharmacometrics Syst. Pharmacol. 10 (4) (2021 Apr) 350–361.
[24] P. Mascheroni, S. Savvopoulos, J.C.L. Alfonso, et al., Improving personalized tumor growth predictions using a Bayesian combination of mechanistic modeling and machine learning, Commun. Med. 1 (2021) 19.
[25] H. Adeli, Z. Zhou, N. Dadmehr, Analysis of EEG records in an epileptic patient using wavelet transform, J. Neurosci. Methods 123 (1) (2003) 69–87.
[26] C.S. Huang, Q.T. Le, W.C. Su, C.H. Chen, Wavelet-based approach of time series model for modal identification of a bridge with incomplete input, Comput. Aided Civ. Infrastruct. Eng. 35 (9) (2020) 947–964.
[27] K. Karami, P. Fatehi, A. Yazdani, On-line system identification of structures using Wavelet-Hilbert transform and sparse component analysis, Comput. Aided Civ. Infrastruct. Eng. 35 (8) (2020) 870–886.

[28] O. Darbin, N. Hatanaka, S. Takara, N. Kaneko, S. Chiken, D. Naritoku, A. Martino, A. Nambu, Parkinsonism differently affects the single neuronal activity in the primary and supplementary motor areas in monkeys: an investigation in linear and nonlinear domains, Int. J. Neural Syst. 30 (2) (2020), 2050010, 25.

[29] D. Avola, M. Cascio, L. Cinque, G.L. Foresti, D. Pannone, Machine learning for video event recognition, Integrated Comput. Aided Eng. 28 (2021) 3.

[30] P. Sharma, Y.U. Khan, O. Farooq, M. Tripathi, H. Adeli, A wavelet-statistical features approach for non-convulsive seizure detection, Clin. EEG Neurosci. 45 (4) (2014) 274–284.

[31] U.R. Acharya, Y. Hagiwara, H. Adeli, Automated Seizure Prediction" Epilepsy & Behavior 88 (2018) 251–261.

[32] P.P. Muhammed Shanir, K.A. Khan, Y.U. Khan, M. Farooq, H. Adeli, Automatic seizure detection based on morphological features using one dimensional local binary pattern on long term EEG, Clin. EEG Neurosci. 49 (5) (2018) 351–362.

[33] H.S. Nogay, H. Adeli, Detection of epileptic seizure using pre-trained deep convolutional neural network and transfer learning, Eur. Neurol. 83 (6) (2020) 602–614.

[34] Z. Sankari, H. Adeli, A. Adeli, Wavelet coherence model for diagnosis of Alzheimer's disease, Clin. EEG Neurosci. 43 (3) (2012) 268–278, 2012.

[35] J.P. Amezquita-Sanchez, A. Adeli, H. Adeli, A new methodology for automated diagnosis of mild cognitive impairment (MCI) using magnetoencephalography (MEG), Behav. Brain Res. 305 (2016) 174–180.

[36] N. Mammone, F.C. Ieracitano, H. Adeli, F.C. Morabito, Permutation Jaccard Distance-based Hierarchical Clustering to estimate EEG network density modifications in MCI subjects, IEEE Transact. Neural Networks Learn. Syst. 29 (10) (2018) 5122–5135.

[37] J.P. Amezquita-Sanchez, N. Mammone, F.C. Morabito, H. Adeli, A new dispersion entropy and fuzzy logic system-based methodology for automated classification of dementia stages using electroencephalograms, Clin. Neurol. Neurosurg. 201 (2021), 106446.

[38] N. Serrano, D. López-Sanz, R. Bruña, P. Garcés, I.C. Rodríguez-Rojo, A. Marcos, D. Prada Crespo, F. Maestú, Spatiotemporal oscillatory patterns during working memory maintenance in mild cognitive impairment and subjective cognitive decline, Int. J. Neural Syst. 30 (1) (2020), 1950019, 18.

[39] T. Hirschauer, H. Adeli, T. Buford, Computer-aided diagnosis of Parkinson's disease using an enhanced probabilistic neural network, J. Med. Syst. 39 (179) (2015) 12.

[40] R. Yuvaraj, M. Murugappan, K. Sundaraj, M.I. Omar, N.M. Ibrahim, K. Mohamad, R. Palaniappan, U.R. Acharya, H. Adeli, E. Mesquita, Brain functional connectivity patterns for emotional state classification in Parkinson's disease patients without dementia, Behav. Brain Res. 298 (2016) 248–260.

[41] S. Bhat, U.R. Acharya, N. Dadmehr, H. Adeli, Parkinson's Disease: cause factors, measurable indicators, and early diagnosis, Comput. Biol. Med. 102 (2018) 234–241, 2018.

[42] P. Vuttipittayamongkol, E. Elyan, Improved overlap-based undersampling for imbalanced dataset classification with application to epilepsy and Parkinson's disease, Int. J. Neural Syst. 30 (8) (2020), 2050043, 21.

[43] J.P. Amezquita-Sanchez, Nadia Mammone, M.C. Morabito, S. Marino, H. Adeli, A novel methodology for automated differential diagnosis of mild cognitive impairment and the Alzheimer's disease using EEG signals, J. Neurosci. Methods 322 (2019) 88–95.

[44] F. Miraglia, F. Vecchio, C. Marra, D. Quaranta, F. Alù, B. Peroni, G. Granata, E. Judica, P.M. Rossini, Small world index in default mode network predicts progression from mild cognitive impairment to dementia, Int. J. Neural Syst. 30 (2) (2020), 2050004, 17.

[45] S. Bhat, U.R. Acharya, H. Adeli, G.M. Muralidhar Bairy, A. Adeli, Automated diagnosis of autism: in search of mathematical markers, 2014, Rev. Neurosci. 25 (6) (2014) 851–861. WOS=38.

[46] S. Bhat, U.R. Acharya, Adeli, G.M. Muralidhar Bairy, A. Adeli, Autism: cause factors, early diagnosis and therapies, 2014, Rev. Neurosci. 25 (6) (2014) 841–850. WOS=79.

[47] H.S. Nogay, H. Adeli, Machine learning (ML) for the diagnosis of autism spectrum disorder (ASD, Using Brain Imaging" Rev. Neurosci. 31 (8) (2020) 825–841.

[48] M. Ahmadlou, H. Adeli, A. Adeli, Spatio-temporal analysis of relative convergence (STARC) of EEGs reveals differences between brain dynamics of depressive women and men, Clin. EEG Neurosci. 44 (2013) 175–181.

[49] U.R. Acharya, S. Vidya, H. Adeli, S. Jayashree, J.E.W. Koh, A. Adeli, Computer aided diagnosis of depression using EEG signals, Eur. Neurol. 73 (2015) 329–336. WOS=73.

[50] U.R. Acharya, S. Vidya, H. Adeli, S. Jayashree, J.E.W. Koh, A. Adeli, A novel depression diagnosis index using nonlinear features in EEG signals, Eur. Neurol. 74 (1–2) (2015) 79–83. WOS=115.

[51] M. Zhu, H. Zhu, F. Guo, Chen, J.W. Ju, Tunnel condition assessment via cloud model-based random forests and self-training approach, Comput. Aided Civ. Infrastruct. Eng. 36 (2) (2021) 164–179.

[52] E. Olejarczyk, U. Zuchowicz, A. Wozniak-Kwasniewska, D. Szekely, O. David, The impact of repetitive transcranial magnetic stimulation on functional connectivity in major depressive and bipolar dosorder evaluated by directed transfer function and indices based on graph theory, Int. J. Neural Syst. 30 (4) (2020), 2050015, 27.

[53] C. Sridhar, S. Bhat, U.R. Acharya, H. Adeli, G.M. Bairy, Diagnosis of attention deficit hyperactivity disorder using imaging and signal processing techniques, Comput. Biol. Med. 88 (2017) 93–99.

[54] L. Wang, X. Li, Y. Zhu, B. Lin, Q. Bo, F. Li, C. Wang, Discriminative analysis of symptom severity and ultra-high risk of schizophrenia using intrinsic functional connectivity, Int. J. Neural Syst. 30 (9) (2020) 2050047.

[55] U.R. Acharya, S. Bhat, O. Faust, H. Adeli, E.C.P. Chua, W.J.E. Lim, J.E.W. Koh, Nonlinear dynamics measure for automated EEG-based sleep stage detection, Eur. Neurol. 74 (2015) 268–287.

[56] U.R. Acharya, S. Vidya, S. Bhat, H. Adeli, A. Adeli, Computer-aided diagnosis of alcoholism-related, E.E.G. Signals " Epilepsy & Behavior 41 (2014) 257–263.

[57] F. Moradi, H. Mohammadi, M. Rezaei, P. Sariaslani, N. Razazian, H. Khazaie, H. Adeli, A novel method for sleep stage classification based on sonification of sleep electroencephalogram signals using wavelet transform and recurrent neural network, Eur. Neurol. 83 (5) (2020) 468–486.

[58] H. Adeli, S. Ghosh-Dastidar, Automated EEG-based diagnosis of neurological disorders - inventing the future of neurology, in: Corroboration with Nahid Dadmehr, C.R.C. Press, Taylor & Francis, Boca Raton, Florida, 2010.

[59] A. Hassanpour, M. Moradikia, H. Adeli, S.R. Khayami, P. Shamsinejad, A novel end-to-end deep learning scheme for classifying multiclass motor imagery EEG signals, 2019, Expet Syst. 36 (2019) 6.

[60] L.C. Lin, C.S. Ouyang, R.C. Wu, R.C. Yang, C.T. Chiang, Alternative diagnosis of epilepsy in children without epileptiform discharges using deep convolutional neural networks, Int. J. Neural Syst. 30 (5) (2020), 1850060, 10.

[61] J. Thomas, J. Jin, P. Thangavel, E. Bagheri, R. Yuvaraj, J. Dauwels, R. Rathakrishnan, J.J. Halford, S.S. Cash, B. Westover, Automated detection of interictal epileptiform discharges from scalp electroencephalograms by convolutional neural networks, Int. J. Neural Syst. 30 (11) (2020), 2050030, 17.

[62] Y. Li, Z. Yu, Y. Chen, C. Yang, Y. Li, X.A. Li, B. Li, Automatic seizure detection using fully convolutional nested LSTM, Int. J. Neural Syst. 30 (4) (2020), 2050019, 22.

[63] G. Liu, W. Zhou, M. Geng, Automatic seizure detection based on S-transform and deep convolutional neural network, Int. J. Neural Syst. 30 (4) (2020), 2050024, 15.

[64] P. Peng, L. Xie, H. Wei, A deep fourier neural network for seizure prediction using convolutional neural network and ratios of spectral power, Int. J. Neural Syst. 31 (8) (2021), 2150022, 20.

[65] Z. Ma, Reachability analysis of neural masses and seizure control based on combination convolutional neural network, Int. J. Neural Syst. 30 (1) (2020), 1950023, 15.

[66] M. Leming, J.M. Gorriz, J. Suckling, Ensemble deep learning on large, mixed-site fMRI datasets in autism and other tasks, Int. J. Neural Syst. 30 (7) (2020) 2050012, 16.

[67] M. Graña, M. Silva, Impact of machine learning pipeline choices in Autism prediction from functional connectivity data, Int. J. Neural Syst. 31 (4) (2021), 2150009, 20.

[68] G. Mirzaei, A. Adeli, H. Adeli, Imaging and machine learning techniques for diagnosis of Alzheimer disease, Rev. Neurosci. 27 (8) (2016) 857–870.

[69] U. Raghavendra, U.R. Acharya, H. Adeli, Artificial intelligence techniques for automated diagnosis of neurological disorders, Eur. Neurol. 82 (2019) 1–3.

[70] K. Tzimourta, V. Christou, A. Tzallas, N. Giannakeas, L. Astrakas, P. Angelidis, D. Tsalikakis, M.G. Tsipouras, Machine learning algorithms and statistical analysis approaches for Alzheimer's disease analysis based on EEG recordings: a systematic review, Int. J. Neural Syst. 31 (5) (2021), 2130002 (33 pages).

[71] M. Przedborski, M. Smalley, S. Thiyagarajan, A. Goldman, M. Kohandel, Systems biology informed neural networks (SBINN) predict response and novel combinations for PD-1 checkpoint blockade, Commun. Biol. 4 (1) (2021 Jul 15) 1–5.

[72] P. Yazdjerdi, N. Meskin, M. Al-Naemi, A.E. Al Moustafa, L. Kovács, Reinforcement learning-based control of tumor growth under anti-angiogenic therapy. Computer methods and programs in biomedicine 173, 2019 May 1, pp. 15–26, 20. Boso DP, Di Mascolo D, Santagiuliana R, Decuzzi P, Schrefler BA. Drug delivery: Experiments, mathematical modelling and machine learning. Computers in Biology and Medicine. 2020 Aug 1;123:103820.

[73] F. Heydarpour, E. Abbasi, M.J. Ebadi, S.M. Karbassi, Solving an optimal control problem of cancer treatment by artificial neural networks, Int. J. Interact. Multimed. Artif. Intell. 6 (4) (2020 Dec 1).

[74] J.N. Eckardt, K. Wendt, M. Bornhäuser, J.M. Middeke, Reinforcement learning for precision oncology, Cancers 13 (18) (2021 Jan) 4624.

[75] A. Yala, P.G. Mikhael, C. Lehman, G. Lin, F. Strand, Y.L. Wan, K. Hughes, S. Satuluru, T. Kim, I. Banerjee, J. Gichoya, Optimizing risk-based breast cancer screening policies with reinforcement learning, Nat. Med. (2022 Jan 13) 1–8.

[76] C.H. Feng, M.L. Disis, C. Cheng, L. Zhang, Multimetric feature selection for analyzing multicategory outcomes of colorectal cancer: random forest and multinomial logistic regression models, Lab. Invest. 102 (3) (2022 Mar) 236–244.

[77] Y. Zhu, X. Wang, K. Mathiak, P. Toiviainen, T. Ristaniemi, J. Xu, Y. Chang, F. Cong, Altered EEG oscillatory brain networks during music-listening in major depression, Int. J. Neural Syst. 31 (3) (2021), 2150001, 14.

[78] S.M. Mousavi, M. Ghasemi, M. Dehghan Manshadi, A. Mosavi, Deep learning for wave energy converter modeling using long short-term memory, Mathematics 9 (8) (2021 Jan) 871.

[79] Manshadi MD, Ghasemi M, Mousavi SM, Mosavi A. Predicting the Related Parameters of Vortex Bladeless Wind Turbine by Using Deep Learning Method.

[80] S. Jemaa, J. Fredrickson, R.A. Carano, T. Nielsen, A. de Crespigny, T. Bengtsson, Tumor segmentation and feature extraction from whole-body FDG-PET/CT using cascaded 2D and 3D convolutional neural networks, J. Digit. Imag. 33 (4) (2020 Aug) 888–894.

[81] A.V. Schperberg, A. Boichard, I.F. Tsigelny, S.B. Richard, R. Kurzrock, Machine learning model to predict oncologic outcomes for drugs in randomized clinical trials, Int. J. Cancer 147 (9) (2020 Nov 1) 2537–2549.

[82] G. DiResta, S. Nathan, M. Manoso, J. Casas-Ganem, C. Wyatt, et al., Cell proliferation of cultured human cancer cells are affected by the elevated tumor pressures that exist in vivo, Ann. Biomed. Eng. 33 (2005) 1270–1280.
[83] S. Nathan, G. DiResta, J. Casas-Ganem, B. Hoang, R. Sowers, et al., Elevated physiologic tumor pressure promotes proliferation and chemosensitivity in human osteosarcoma, Clin. Cancer Res. 11 (2005) 2389–2397.
[84] M. Hofmann, M. Guschel, A. Bernd, J. Bereiter-Hahn, R. Kaufmann, et al., Lowering of tumor interstitial fluid pressure reduces tumor cell proliferation in axenograft tumor model, Neoplasia 8 (2006) 89–95.
[85] C. Heldin, K. Rubin, K. Pietras, A. O stman, High interstitial fluid pressure -an obstacle in cancer therapy, Nat. Rev. Cancer 4 (2004) 806–813.
[86] H. Wiig, O. Tenstad, P. Iversen, R. Kalluri, R. Bjerkvig, Interstitial fluid: the overlooked component of the tumor microenvironment, Fibrogenesis Tissue Repair 3 (2010).
[87] N. Srikantha, K. Suhling, T. Jackson, Translational diffusion of ranibizumab and bevacizumab as measured by Fluorescence Recovery after Photobleaching (FRAP), Investig. Ophthalmol. Vis. Sci. 53 (14) (2012 Mar 26) 6488.
[88] Q.D. Nguyen, A. Das, D.V. Do, P.U. Dugel, A. Gomes, F.G. Holz, A. Koh, C.K. Pan, Y.J. Sepah, N. Patel, H. MacLeod, Brolucizumab: evolution through preclinical and clinical studies and the implications for the management of neovascular age-related macular degeneration, Ophthalmology 127 (7) (2020 Jul 1) 963–976.
[89] L.T. Baxter, R.K. Jain, Transport of fluid and macromolecules in tumors. I. Role of interstitial pressure and convection, Microvasc. Res. 37 (1) (1989 Jan 1) 77–104.
[90] J.C. Luo, S. Yamaguchi, A. Shinkai, K. Shitara, M. Shibuya, Significant expression of vascular endothelial growth factor/vascular permeability factor in mouse ascites tumors, Cancer Res. 58 (12) (1998 Jun 15) 2652–2660.
[91] A. Botchkarev, A new topology design of performance metrics to measure errors in machine learning regression algorithms, Interdiscipl. J. Inf. Knowl. Manag. (2019 Jan 1) 14.
[92] V.W. van Hinsbergh, Angiogenesis: basics of vascular biology, Vascular iz. Tissue Eng. Regen. Med. 3–1 (2021).
[93] N. Kuriyama, Y. Yoshioka, S. Kikuchi, N. Azuma, T. Ochiya, Extracellular vesicles are key regulators of tumor neovasculature, Front. Cell Dev. Biol. 8 (2020 Dec 9) 1510.
[94] C.M. Phillips, E.A. Lima, R.T. Woodall, A. Brock, T.E. Yankeelov, A hybrid model of tumor growth and angiogenesis: in silico experiments, PLoS One 15 (4) (2020 Apr 10), e0231137.
[95] J.P. Alberding, T.W. Secomb, Simulation of angiogenesis in three dimensions: application to cerebral cortex, PLoS Comput. Biol. 17 (6) (2021 Jun 25), e1009164.
[96] M. Dey, B. Ayan, M. Yurieva, D. Unutmaz, I.T. Ozbolat, Studying tumor angiogenesis and cancer invasion in a three-dimensional vascularized breast cancer micro-environment, Adv. Biol. (2021 Apr 15), 2100090.
[97] B.J. Vakoc, R.M. Lanning, J.A. Tyrrell, T.P. Padera, L.A. Bartlett, T. Stylianopoulos, L.L. Munn, G.J. Tearney, D. Fukumura, R.K. Jain, Bouma BE Three-dimensional microscopy of the tumor microenvironment in vivo using optical frequency domain imaging, Nat. Med. 15 (10) (2009 Oct) 1219–1223.
[98] F. Roudnicky, S.Y. Yoon, S. Poghosyan, S. Schwager, C. Poyet, G. Vella, S. B. Bachmann, S. Karaman, J.W. Shin, V.I. Otto, M. Detmar, Alternative transcription of a shorter, non-anti-angiogenic thrombospondin-2 variant in cancer-associated blood vessels, Oncogene 37 (19) (2018 May) 2573–2585.
[99] H.-L. Chen, G. Wang, C. Ma, Z.-N. Cai, W.-B. Liu, S.-J. Wang, An efficient hybrid kernel extreme learning machine approach for early diagnosis of Parkinson's disease, Neurocomputing 184 (2016) 131–144.
[100] J. Hu, et al., Orthogonal learning covariance matrix for defects of grey wolf optimizer: insights, balance, diversity, and feature selection, Knowl. Base Syst. 213 (2021), 106684.
[101] Y. Zhang, et al., Towards Augmented Kernel Extreme Learning Models for Bankruptcy Prediction: Algorithmic Behavior and Comprehensive Analysis, Neurocomputing, 2020.
[102] D. Zhao, et al., Chaotic Random Spare Ant Colony Optimization for Multi-Threshold Image Segmentation of 2D Kapur Entropy, Knowledge-Based Systems, 2020, 106510.
[103] J. Tu, et al., Evolutionary Biogeography-Based Whale Optimization Methods with Communication Structure: towards Measuring the Balance, Knowledge-Based Systems, 2020, 106642.
[104] W. Shan, et al., Double Adaptive Weights for Stabilization of Moth Flame Optimizer: Balance Analysis, Engineering Cases, and Medical Diagnosis, Knowledge-Based Systems, 2020, 106728.